

A Gas-Kinetic Scheme for Maxwell Equations

Zhigang PU^a, Kun XU^{a,b,*}

^a*Department of Mathematics, Hong Kong University of Science and Technology, Clear Water Bay, Kowloon, Hong Kong, China*

^b*Shenzhen Research Institute, Hong Kong University of Science and Technology, Shenzhen, China*

Abstract

In this paper, we present a gas-kinetic scheme using discrete velocity space to solve Maxwell equations. The kinetic model recovers Maxwell equations in the zero relaxation time limit. The scheme achieves second-order spatial and temporal accuracy in structured meshes comparable to the finite-difference time-domain (FDTD) method, without requiring staggered grids or leapfrog discretization. Our kinetic scheme is inherently multidimensional due to its use of kinetic beams in multiple directions, allowing larger time steps in multidimensional computations. It demonstrates better stability than FDTD when handling discontinuities and readily extends to unstructured meshes. We validate the method through various test cases including antenna simulation, sphere scattering, and flight vehicle scattering. The results align well with Riemann-solver-based solutions. Finally, we examine charge conservation for Maxwell equations through test cases.

Keywords: , Gas-kinetic scheme, Maxwell equations, Kinetic solver

1. Introduction

Numerical methods for solving Maxwell's equations are fundamental to computational electromagnetics (CEM). The development of accurate and efficient numerical methods serves both practical applications and basic research needs. These methods are crucial for designing and modeling communication systems, including antennas, radars, and satellites, while also being essential for simulating fundamental physical processes such as laser-plasma interactions, inductively coupled plasma, and helicon wave plasma. Among the most commonly used approaches are the finite-difference time-domain (FDTD) method, finite element method (FEM), and finite volume method (FVM), each with distinct advantages and limitations.

The FDTD method is widely utilized in computational electromagnetics for its simplicity and efficiency. It employs staggered Yee grid arrangements to satisfy elliptical divergence constraints, with electric and magnetic fields defined at staggered grid points and updated in a leapfrog manner. This approach achieves second-order accuracy in both time and space [1, 2]. While Holland extended the Yee algorithm to curvilinear structured mesh [3], the FDTD method faces challenges when applied to unstructured meshes for complex geometries [4].

FEM offers greater flexibility in handling complex geometries than FDTD. Based on weak formulations of Maxwell's equations in the frequency domain [5], FEM uses edge elements introduced by Nédélec to address spurious modes caused by nodal basis functions [6]. These

*Cooresponding author

Email addresses: zpuac@connect.ust.hk (Zhigang PU), makxu@ust.hk (Kun XU)

elements allow discontinuities in normal components across interfaces while maintaining tangential component continuity. A limitation of FEM is its requirement to solve a sparse linear system at each time step, though techniques like mass lumping have been developed to simplify the mass matrix to diagonal form [7]. Similar to FEM, the method of moments (MoM) solves the integral form of Maxwell equations [8, 9]. For materials with spatially varying electromagnetic properties or inhomogeneities, differential Maxwell systems are preferred over integral equations [10].

FVM, initially developed for nonlinear hyperbolic systems in fluid dynamics [11, 12], integrates equations over mesh cells where cell-averaged quantities evolve based on interface fluxes calculated through Riemann problems [13]. Mohammadian achieved second-order accuracy for Maxwell equations using the Lax-Wendroff scheme [14], while Shang obtained higher-order spatial accuracy using flux vector splitting and the MUSCL scheme [15]. The characteristic-based Riemann solution effectively handles boundary conditions for infinitely outgoing waves, preventing spurious reflections. Munz introduced perfect hyperbolic Maxwell (PHM) equations to control divergence error in particle-in-cell (PIC) simulations and later integrated PHM into the FVM framework [16, 17, 18]. The discontinuous Galerkin (DG) method combines FVM and FEM to avoid complex reconstruction for higher spatial accuracy [19]. While DG with explicit Runge-Kutta time integration faces restrictive CFL conditions [20], implicit methods like the kinetic implicit scheme help overcome these limitations [21]. In computational electromagnetics, the finite volume formulation using integral form of Maxwell’s equations is known as the finite integration method (FIT) [22]. Initially developed independently of FDTD and later expanded as its generalization [23, 24], FIT employs staggered grids but uses numerical flux based on integral form of Maxwell’s equation rather than Riemann solutions. FIT provides greater flexibility in grid selection for complex geometries and eliminates the need for reconstruction through dual grids [25].

Since both Maxwell’s equations and fluid dynamics involve hyperbolic systems, methods from computational fluid dynamics (CFD) can be adapted for electromagnetic computations. Beyond Riemann-solver-based FVM methods, kinetic-solver-based approaches provide concise formulations for multidimensional hyperbolic systems without requiring local Riemann problem solutions [26]. In fluid dynamics, prominent kinetic theory-based methods include the Gas-Kinetic Scheme (GKS) [27, 28], which uses continuous velocity space, and the Lattice Boltzmann Method (LBM) [29, 30], which employs discrete velocity space. These kinetic models offer simpler formulations for multidimensional systems compared to Riemann-solver-based schemes. In GKS, the BGK equation’s integral solution at cell interfaces extends directly to multiple dimensions, while LBM achieves true multidimensionality through isotropic lattice velocity distribution and precise transport operators. These approaches facilitate implicit and parallel algorithms with straightforward implementation [31, 32, 26]. Kinetic models for Maxwell equations provide a consistent framework when coupling with the kinetic formulation based nonequilibrium flow solver [33]. Despite the advantage, kinetic model extensions to Maxwell systems remain limited. Gerhard’s work approximates Maxwell systems using discrete kinetic models solved with DG methods [21, 34], primarily to enable sweep algorithms for large time steps instead of solving large linear systems in classical implicit schemes. The full potential of kinetic models’ multidimensional capabilities remains unexplored in this context.

Here we develop numerical methods using discrete kinetic models for Maxwell equations (PHM equations). The approach achieves second-order accuracy in space and time like FDTD on structured meshes, but without requiring staggered grids or leapfrog updates. The kinetic

formulation provides true multidimensionality and enhanced stability for discontinuities compared to FDTD. The method extends to unstructured meshes for complex geometries and has been validated through antenna simulations, sphere scattering, and flight vehicle scattering cases, showing good agreement with Riemann-solver-based FVM results.

The structure of this paper is outlined as follows. Section 2 introduces the kinetic representation of the Maxwell system. Section 3 presents the numerical algorithms for both structured and unstructured meshes. section 5 is about the asymptotic analysis of the one-dimensional polarized Maxwell equation and the derivation of the first-order equivalent equation with respect to both the relaxation parameter τ and the time step Δt . Following this, a series of numerical tests are presented. Section 6.1 evaluates the convergence order. In section 6.2, the multidimensionality property is demonstrated, and the capability to handle discontinuities is shown. In section 6.3 to section 6.5, various test cases in the unstructured mesh are presented. Finally, we conclude the paper in section 7.

2. Kinetic representation of Maxwell system

2.1. Maxwell system

The PHM equations are used here for divergence cleaning,

$$\frac{\partial \mathbf{E}}{\partial t} - c^2 \nabla_{\mathbf{x}} \times \mathbf{B} + \chi c^2 \nabla_{\mathbf{x}} \phi = -\frac{1}{\epsilon_0} \mathbf{J}, \quad (1)$$

$$\frac{\partial \mathbf{B}}{\partial t} + \nabla_{\mathbf{x}} \times \mathbf{E} + \gamma \nabla_{\mathbf{x}} \psi = 0, \quad (2)$$

$$\frac{1}{\chi} \frac{\partial \phi}{\partial t} + \nabla_{\mathbf{x}} \cdot \mathbf{E} = \frac{q}{\epsilon_0}, \quad (3)$$

$$\frac{\epsilon_0 \mu_0}{\gamma} \frac{\partial \psi}{\partial t} + \nabla_{\mathbf{x}} \cdot \mathbf{B} = 0, \quad (4)$$

where ϕ, ψ are artificial correction potentials to accommodate divergence errors traveling at speed γc and χc [16]. To construct a finite-volume scheme, we rewrite Eqs.(1), (2), (3) and (4) as a system of linear hyperbolic evolution equations

$$\frac{\partial \mathbf{U}}{\partial t} + \nabla \cdot \mathbb{F}(\mathbf{U}) = \mathbf{S}(\mathbf{U}), \quad (5)$$

where $\mathbf{U} \in \mathbb{R}^8$ is the vector of unknowns given by

$$\mathbf{U} = (E_x, E_y, E_z, B_x, B_y, B_z, \phi, \psi)^T, \quad (6)$$

and $\mathbb{F}(\mathbf{U}) = (\mathbf{F}_1(\mathbf{U}), \mathbf{F}_2(\mathbf{U}), \mathbf{F}_3(\mathbf{U})) \in \mathbb{R}^{8 \times 3}$ is the flux tensor. The flux function along j direction $\mathbf{F}_j(\mathbf{U}) = \mathbb{A}_j \mathbf{U}$, the Jacobian matrixs $\mathbb{A}_j \in \mathbb{R}^{8 \times 8}$ with constant entries are defined as

$$\mathbb{A}_j = \begin{pmatrix} 0 & 0 & 0 & & & \chi c^2 \delta_{1j} & 0 \\ 0 & 0 & 0 & & c^2 \mathbb{M}_j & \chi c^2 \delta_{2j} & 0 \\ 0 & 0 & 0 & & & \chi c^2 \delta_{3j} & 0 \\ & & & 0 & 0 & 0 & \gamma \delta_{1j} \\ & \mathbb{M}_j^T & & 0 & 0 & 0 & \gamma \delta_{2j} \\ & & & 0 & 0 & 0 & 0 \\ \chi \delta_{1j} & \chi \delta_{2j} & \chi \delta_{3j} & 0 & 0 & 0 & 0 \\ 0 & 0 & 0 & \gamma c^2 \delta_{1j} & \gamma c^2 \delta_{2j} & \gamma c^2 \delta_{3j} & 0 \end{pmatrix}; \quad j = 1, 2, 3, \quad (7)$$

where δ_{ij} denotes the usual Kronecker symbol and the two 3×3 matrices \mathbb{M}_j are found to be

$$\mathbb{M}_1 = \begin{pmatrix} 0 & 0 & 0 \\ 0 & 0 & 1 \\ 0 & -1 & 0 \end{pmatrix}, \quad \mathbb{M}_2 = \begin{pmatrix} 0 & 0 & -1 \\ 0 & 0 & 0 \\ 1 & 0 & 0 \end{pmatrix}, \quad \mathbb{M}_3 = \begin{pmatrix} 0 & 1 & 0 \\ -1 & 0 & 0 \\ 0 & 0 & 0 \end{pmatrix}.$$

The source term reads as

$$\mathbf{S}(\mathbf{U}) = (-J_x/\epsilon_0, -J_y/\epsilon_0, -J_z/\epsilon_0, 0, 0, 0, \chi\rho/\epsilon_0, 0)^T. \quad (8)$$

2.2. Kinetic representation

In the gas kinetic theory, the Boltzmann equation is used to describe the evolution of the distribution function of particles in phase space. An approximate relaxation model is the BGK equation,

$$\frac{\partial f}{\partial t} + \mathbf{u} \cdot \nabla f = \frac{g - f}{\tau},$$

where $f(\mathbf{x}, \mathbf{u}, t)$ is the scalar distribution function at the physical space \mathbf{x} and the velocity space $\mathbf{u} = (u, v, w)$. Here g is the local thermal equilibrium (LTE) distribution determined by the macroscopic quantities, such as the density, velocity, and temperature. τ is the relaxation parameter. The macroscopic Navier-Stokes equations can be derived from the BGK equation in the hydrodynamic limit through the Chapman-Enskog expansion [35].

To develop a kinetic model for the Maxwell system, two key adaptations are necessary. First, the velocity space must be discretized. Unlike gases, where an infinite number of particles follow infinite characteristic lines, electromagnetic waves propagate along a finite number of characteristics, resulting in a limited set of microscopic velocities. We can represent the propagation of electromagnetic waves using a set of discrete beams, following the Beam scheme [36, 37] and the LBM. Second, the asymmetry of \mathbb{F} in Eq. (7) precludes the construction of a scalar distribution function for the system [38]. Following Bouchut [39], we introduce a vector-valued distribution function $\mathbf{f}(\mathbf{x}, \mathbf{v}_k, t) \in \mathbb{R}^{8 \times 1}$ for the system,

$$\sum_{k=1}^M \mathbf{f}_k(\mathbf{x}, \mathbf{v}_k, t) = \mathbf{U}(\mathbf{x}, t), \quad (9)$$

where $\mathbf{v}_k \in \mathbb{R}^{3 \times 1}$ is the k th discrete kinetic velocity vector, M is the total number of discrete kinetic velocities. The discretized BGK kinetic equation is given as:

$$\frac{\partial \mathbf{f}_k}{\partial t} + \mathbf{v}_k \cdot \nabla \mathbf{f}_k = \frac{\mathbf{g}_k - \mathbf{f}_k}{\tau}, \quad (10)$$

where $\mathbf{g}_k = \mathbf{g}(\mathbf{x}, \mathbf{v}_k, t) \in \mathbb{R}^{8 \times 1}$ is the LTE distribution function corresponding to the discrete velocity \mathbf{v}_k . To find the expression of \mathbf{g}_k , in the limit $\tau \rightarrow 0$ the microscopic system Eq.(10) should recover the macroscopic system (5). In such a limit, with the local equilibrium assumption $\mathbf{f}_k = \mathbf{g}_k$, the distribution must satisfy the following compatibility constraints

$$\sum_{k=1}^M \mathbf{g}_k = \mathbf{U}, \quad \sum_{k=1}^M \mathbf{g}_k \otimes \mathbf{v}_k = \mathbb{F}(\mathbf{U}). \quad (11)$$

A natural choice for \mathbf{g}_k is,

$$\mathbf{g}_k = w_k(\mathbf{U} + \Theta^{-1}\mathbb{F}(\mathbf{U}) \cdot \mathbf{v}_k), \quad (12)$$

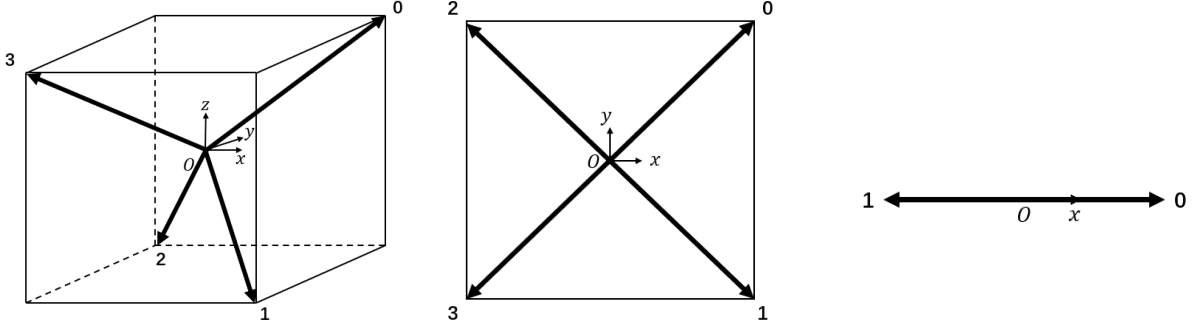


Figure 1: The lattice structure of D3Q4, D2Q4 and D1Q2.

where w_k is the weight, Θ is the temperature. In this work, k is equal to 4 to satisfy the 4 constraints for g_j in Eq.(11). The four kinetic velocities are chosen as

$$\mathbf{v}_0 = \begin{pmatrix} \lambda \\ \lambda \\ \lambda \end{pmatrix} c, \quad \mathbf{v}_1 = \begin{pmatrix} \lambda \\ -\lambda \\ -\lambda \end{pmatrix} c, \quad \mathbf{v}_2 = \begin{pmatrix} -\lambda \\ \lambda \\ -\lambda \end{pmatrix} c, \quad \mathbf{v}_3 = \begin{pmatrix} -\lambda \\ -\lambda \\ \lambda \end{pmatrix} c, \quad (13)$$

where c is the speed of light, λ is the coefficient to adjust the microscopic kinetic velocity. According to the sub-characteristic condition [40], $\lambda > 1$ is required for the kinetic approximation to be dissipative, which is beneficial for stability. The LTE coefficients under such conditions can be calculated as

$$\mathbf{g}_k = \frac{\mathbf{U}_k}{4} + \frac{1}{4\lambda^2 c^2} \mathbb{F}(\mathbf{U}) \cdot \mathbf{v}_k. \quad (14)$$

This lattice automatically degenerates to D2Q4 in 2D and D1Q2 in 1D. The choice of lattice here lacks of symmetry, which distinguishes it from classical LBM. This asymmetry arises from the fundamentally different microscopic nature of electromagnetic waves compared to hydrodynamics. Unlike in fluid dynamics, having more beams for the Maxwell system in various directions may not necessarily enhance the accuracy and stability of the kinetic model.

3. Algorithms

3.1. General steps

The operator-splitting method is employed to solve the kinetic model Eq.(10),

$$\begin{cases} \mathcal{R}(\Delta t) : \frac{\partial \mathbf{f}_k}{\partial t} = \frac{\mathbf{g}_k - \mathbf{f}_k}{\tau}, \\ \mathcal{T}(\Delta t) : \frac{\partial \mathbf{f}_k}{\partial t} + \mathbf{v}_k \cdot \nabla \mathbf{f}_k = 0, \end{cases} \quad (15)$$

where \mathcal{R} means collision relaxation operator, which is a local homogeneous relaxation term. \mathcal{T} means transport operator.

For the collision operator \mathcal{R} , the Crank-Nicolson scheme is employed.

$$\mathbf{f}_{k,i}^* = \frac{1 - \frac{\Delta t}{2\tau}}{1 + \frac{\Delta t}{2\tau}} \mathbf{f}_{k,i}^n + \frac{\frac{2\Delta t}{\tau}}{1 + \frac{\Delta t}{2\tau}} \mathbf{g}_{k,i}^n \xrightarrow{\omega = \frac{2\Delta t}{\tau}} (1 - \omega) \mathbf{f}_{k,i}^n + \omega \mathbf{g}_{k,i}^n, \quad (16)$$

where i is the cell index. For the transport operator \mathcal{T} , either the exact solution or the corner transport upwind (CTU) scheme can be utilized on structured meshes while the upwind flux is applied on unstructured meshes. This will be explained in detail later. After the transport step, map the microscopic distribution function to the macroscopic quantities by the following formula

$$U_i^* = \sum_k f_k.$$

Finally, the solution is updated with the inclusion of the source term,

$$U^{n+1} = U^* + \Delta t \mathcal{S}(U^{n+1/2}). \quad (17)$$

The general steps are as follows:

1. **Collision process:** update microscopic distribution function from $f_{k,i}^n$ to $f_{k,i}^*$ for the collision process.
2. **Transport process:** update microscopic distribution function from $f_{k,i}^*$ to $f_{k,i}^{n+1}$ for the transport process.
3. **Micro-macro mapping:** update macroscopic distribution function from U_i^n to U_i^* .
4. **Source term:** update macroscopic distribution function from U_i^* to U_i^{n+1} .

Up to this point, both microscopic and macroscopic variables are updated from t^n to t^{n+1} .

3.2. Transport operator in structured meshes

In structured meshes, the transport operator can be solved exactly or by the upwind scheme in the framework of the finite volume method. Since the transport equation is linear, the analytical solution based on the characteristic theory can be obtained. The solution is

$$f_k(\mathbf{x}, t + \Delta t) = f_k(\mathbf{x} - \mathbf{v}_k \Delta t, t). \quad (18)$$

Let $\Delta \mathbf{x} / \Delta t = |\mathbf{v}_k|$, Eq.(18) can be written as

$$f_k(\mathbf{x}, t + \Delta t) = f_k(\mathbf{x} - \hat{e}_k \Delta x, t), \quad (19)$$

where \hat{e}_k is the unit direction vector of microscopic velocity \mathbf{v}_k . The Eq.(19) is the same as the LBM transport operator. This method is referred as the Beam-ET method, where "ET" stands for "Exact Transport". Solving the transport equation exactly realizes the multidimensionality of the scheme. However, this method is hardly generalized into unstructured meshes.

Compared to the exact solution, the upwind scheme is more flexible and can be easily extended to unstructured mesh. In the framework of FVM, the cell averaged distribution function values $f_{k,i}$ on a physical cell Ω_i are defined as

$$f_{k,i} = \frac{1}{|\Omega_i|} \int_{\Omega_i} f_k(\mathbf{x}) d\mathbf{x}.$$

The normal numerical flux $\mathcal{F}_{k,i+1/2,j}$ of f_k across interface $(i + 1/2, j)$ is calculated according to the upwind scheme as

$$\mathcal{F}_{k,i+1/2,j} = \begin{cases} f_{k,i,j}(\mathbf{v}_k \cdot \hat{e}_x), & \text{if } \mathbf{v}_k \cdot \hat{e}_x > 0, \\ f_{k,i+1,j}(\mathbf{v}_k \cdot \hat{e}_x), & \text{if } \mathbf{v}_k \cdot \hat{e}_x < 0, \end{cases}$$

where cell interface $(i + 1/2, j)$ is the interface between cell (i, j) and $(i + 1, j)$. To incorporate the multidimensional effect, a transverse correction is added according to the idea of corner transport upwind (CTU) by Collela [41],

$$\mathcal{F}_{k,i+1/2,j} = \begin{cases} \mathbf{f}_{k,i,j}^*(\mathbf{v}_k \cdot \hat{e}_x), & \text{if } \mathbf{v}_k \cdot \hat{e}_x > 0, \\ \mathbf{f}_{k,i+1,j}^*(\mathbf{v}_k \cdot \hat{e}_x), & \text{if } \mathbf{v}_k \cdot \hat{e}_x < 0, \end{cases}$$

where,

$$\mathbf{f}_{k,i,j}^* = \begin{cases} \mathbf{f}_{k,i,j} + \frac{(\mathbf{v}_k \cdot \hat{e}_y)\Delta t}{2\Delta y}(\mathbf{f}_{k,i-1,j} - \mathbf{f}_{k,i,j}), & \text{if } \mathbf{v}_k \cdot \hat{e}_y > 0, \\ \mathbf{f}_{k,i,j} + \frac{(\mathbf{v}_k \cdot \hat{e}_y)\Delta t}{2\Delta y}(\mathbf{f}_{k,i,j} - \mathbf{f}_{k,i+1,j}), & \text{if } \mathbf{v}_k \cdot \hat{e}_y < 0. \end{cases}$$

For the numerical flux across interface $(i, j + 1/2)$, the similar procedure is applied. For the 3D case, the transverse correction needs to incorporate velocity in the z -direction. We refer to this method as the Beam-CTU method. The Beam-CTU method is a simple and efficient way to incorporate multidimensional effects into the upwind scheme. It can be easily proved that if $\Delta \mathbf{x}/\Delta t = |\mathbf{v}_k|$ the Beam-CTU method is equivalent to the Beam-ET method.

3.3. Transport operator on unstructured meshes

In the framework of FVM. The cell averaged distribution function values $\mathbf{f}_{k,i}$ on a physical cell Ω_i are defined as

$$\mathbf{f}_{k,i} = \frac{1}{|\Omega_i|} \int_{\Omega_i} \mathbf{f}_k(\mathbf{x}) d\mathbf{x},$$

where $|\Omega_i|$ is the volume of cell Ω_i . For a discretized time step $\Delta t = t^{n+1} - t^n$, the evolution of $\mathbf{f}_{k,i}$ is

$$\mathbf{f}_{k,i}^{n+1} = \mathbf{f}_{k,i}^n - \frac{\Delta t}{|\Omega_i|} \sum_{s \in \partial\Omega_i} |l_s| \mathcal{F}_s + \Delta t \mathbf{S}_i^{n+1}, \quad (20)$$

where $l_s \in \partial\Omega_i$ is the cell interface with center \mathbf{x}_s and outer unit normal vector \mathbf{n}_s . $|l_s|$ is the area of the cell interface. \mathbf{S}_i is the source term. \mathcal{F}_s is the numerical flux across interface l_s , evaluated as

$$\mathcal{F}_s = \mathbf{f}_{k,i}^n(\mathbf{v}_k \cdot \mathbf{n}_s)_+ + \mathbf{f}_{k,N}^n(\mathbf{v}_k \cdot \mathbf{n}_s)_-, \quad (21)$$

where $(a)_+ = \max(a, 0)$, $(a)_- = \min(a, 0)$, N is the neighbor cell sharing interface $\partial\Omega_i$. To improve the spatial accuracy, the Green-Gauss method or the Least-Squares method can be employed to calculate the average gradient within each cell. These gradients are then used to reconstruct the variables at the cell interfaces.

3.4. Summary

The algorithms introduced above are summarised in the table below:

Method	Transport solver	Mesh type
Beam-ET	Exact transport	Structured
Beam-CTU	CTU method	Structured
Beam-U	Upwind method	Unstructured

Table 1: Summary of Beam-ET, Beam-CTU, Beam-U methods.

4. Flux vector splitting scheme for PHM system

In this section, we demonstrate a Riemann-solver-based finite volume method for the PHM system. This method employs operator splitting to handle multidimensional cases, which means that the numerical fluxes only contain waves normal to the cell interfaces. We will use the results obtained from this method as a reference for comparison with the kinetic-solver-based method.

In the framework of the FVM, the cell averaged variables $\mathbf{U}_i = (E_{xi}, E_{yi}, E_{zi}, B_{xi}, B_{yi}, B_{zi}, \phi, \psi)$ on a physical cell Ω_i are defined as

$$\mathbf{U}_i = \frac{1}{|\Omega_i|} \int_{\Omega_i} \mathbf{U}(\mathbf{x}) d\mathbf{x},$$

where $|\Omega_i|$ is the volume of cell Ω_i . For a discretized time step $\Delta t = t^{n+1} - t^n$, the evolution of \mathbf{U}_i is

$$\mathbf{U}_i^{n+1} = \mathbf{U}_i^n - \frac{\Delta t}{|\Omega_i|} \sum_{s \in \partial\Omega_i} |l_s| \mathcal{F}_s \cdot \mathbf{n}_s + \Delta t \mathbf{S}_i^{n+1}, \quad (22)$$

where $l_s \in \partial\Omega_i$ is the cell interface with center \mathbf{x}_s and outer unit normal vector \mathbf{n}_s . $|l_s|$ is the area of the cell interface. The numerical flux across interface \mathcal{F}_s can be evaluated by coordinate transformation,

$$\mathcal{F}_s \cdot \mathbf{n}_s = \mathbb{T}^{-1}[\widetilde{\mathcal{F}}_s(\mathbb{T}\mathbf{U}) \cdot \widetilde{\mathbf{n}}_s] = \mathbb{T}^{-1}[\widetilde{\mathcal{F}}_s(\widetilde{\mathbf{U}}) \cdot \widetilde{\mathbf{n}}_s],$$

where $\mathbb{T} = \text{diag}(1, \mathbb{T}', 1)$ is a rotating operator, transforming the global coordinate system into a local coordinate system, and

$$\mathbb{T}' = \begin{pmatrix} n_1 & n_2 & n_3 \\ -n_2 & n_1 + \frac{n_3^2}{1+n_1} & -\frac{n_2 n_3}{1+n_1} \\ -n_3 & -\frac{n_2 n_3}{1+n_1} & 1 - \frac{n_3^2}{1+n_1} \end{pmatrix}, \quad n_1 \neq -1,$$

when $n_1 = -1$, $\mathbb{T}' = \text{diag}(-1, -1, 1)$. $\widetilde{\mathcal{F}}_s$ means numerical flux in the local coordinate system, $\widetilde{\mathbf{U}}$ means variables in the local coordinate system. Operator \mathbb{T}^{-1} transforms the local coordinate system to the global coordinate system. In the local coordinate system, the normal vector aligns with x -direction $\widetilde{\mathbf{n}}_s = \hat{e}_x$. Therefore, only flux along x -direction needs to be considered, which is given by the following equation

$$\frac{\partial \mathbf{U}}{\partial t} + \mathbb{A}_1 \frac{\partial \mathbf{U}}{\partial x} = \mathbf{S}(\mathbf{U}), \quad (23)$$

where

$$\mathbb{A}_1 = \begin{pmatrix} 0 & 0 & 0 & 0 & 0 & 0 & c^2 \chi & 0 \\ 0 & 0 & 0 & 0 & 0 & c^2 & 0 & 0 \\ 0 & 0 & 0 & 0 & -c^2 & 0 & 0 & 0 \\ 0 & 0 & 0 & 0 & 0 & 0 & 0 & \gamma \\ 0 & 0 & -1 & 0 & 0 & 0 & 0 & 0 \\ 0 & 1 & 0 & 0 & 0 & 0 & 0 & 0 \\ \chi & 0 & 0 & 0 & 0 & 0 & 0 & 0 \\ 0 & 0 & 0 & c^2 \gamma & 0 & 0 & 0 & 0 \end{pmatrix}.$$

Eq.(23) is a linear system whose Riemann solution can be accurately captured without iteration. We can use the upwind scheme to calculate the numerical flux,

$$\mathcal{F}_s(\mathbf{U}_L, \mathbf{U}_R) = \frac{1}{2}\mathbb{A}_1(\mathbf{U}_L + \mathbf{U}_R) - \frac{1}{2}|\mathbb{A}_1|(\mathbf{U}_R - \mathbf{U}_L),$$

where $|\mathbb{A}_1| = \mathbb{A}_1^+ - \mathbb{A}_1^-$ and $\mathbb{A}_1^\pm = \mathbb{R}\Lambda^\pm\mathbb{R}^{-1}$, $\Lambda^\pm = \text{diag}(\lambda_1^\pm, \dots, \lambda_8^\pm)$. λ_m is the m -th eigenvalue of \mathbb{A}_1 , and $\lambda_m^\pm = \frac{1}{2}(\lambda_m \pm |\lambda_m|)$. $\mathbb{R} = [\mathbf{r}_1, \dots, \mathbf{r}_8]$ is the matrix composed by right eigenvectors. To achieve second-order spatial accuracy, the Green-Gauss method or the Least-Squares method can be employed to calculate the average gradient within each cell. These gradients are then used to reconstruct the variables at the cell interfaces. The source terms are handled using operator splitting.

5. Asymptotic analysis

In this section, we employ a one-dimensional (1-D) polarized pure electromagnetic wave equation to illustrate the asymptotic behavior of the kinetic model and the numerical method. The kinetic behaviors and temporal accuracy are explored through this analysis.

The 1-D equation can be written as:

$$\begin{aligned} \frac{\partial E_y}{\partial t} + c^2 \frac{\partial B_z}{\partial x} &= 0, \\ \frac{\partial B_z}{\partial t} + \frac{\partial E_y}{\partial x} &= 0. \end{aligned} \tag{24}$$

In this system,

$$\mathbf{U} = (E_y, B_z)^T, \quad \mathbb{F}(\mathbf{U}) \equiv \mathbf{F}_1(\mathbf{U}) = (c^2 B_z, E_y)^T,$$

and the Jacobian is

$$\mathbb{A} = \begin{pmatrix} 0 & c^2 \\ 1 & 1 \end{pmatrix}.$$

In this case, we can choose $k = 2$ kinetic velocities to approximate the Eq.(24),

$$\mathbf{v} = (v_1, v_2)^T = (\lambda, -\lambda)^T c.$$

The discrete equilibrium distribution can be expressed as,

$$\mathbf{g} = \begin{pmatrix} g_{E_y,1} & g_{E_y,2} \\ g_{B_z,1} & g_{B_z,2} \end{pmatrix} = \begin{pmatrix} \frac{1}{2}(E_y + \frac{cB_z}{\lambda}) & \frac{1}{2}(E_y - \frac{cB_z}{\lambda}) \\ \frac{1}{2}(B_z + \frac{E_y}{\lambda c}) & \frac{1}{2}(B_z - \frac{E_y}{\lambda c}) \end{pmatrix} \tag{25}$$

The kinetic evolution system is

$$\frac{\partial \mathbf{f}_2}{\partial t} - \lambda c \frac{\partial \mathbf{f}_1}{\partial x} = \frac{\mathbf{g}_1 - \mathbf{f}_1}{\tau}, \quad \frac{\partial \mathbf{f}_2}{\partial t} + \lambda c \frac{\partial \mathbf{f}_2}{\partial x} = \frac{\mathbf{g}_2 - \mathbf{f}_2}{\tau},$$

where $\mathbf{f}_k \equiv (f_{E_y,k}, f_{B_z,k})$. Consider the equation of E_y first,

$$\frac{\partial f_{E_y,1}}{\partial t} - \lambda c \frac{\partial f_{E_y,1}}{\partial x} = \frac{g_{E_y,1} - f_{E_y,1}}{\tau}, \tag{26}$$

$$\frac{\partial f_{E_y,2}}{\partial t} + \lambda c \frac{\partial f_{E_y,2}}{\partial x} = \frac{g_{E_y,2} - f_{E_y,2}}{\tau}, \tag{27}$$

According to Eq.(9), $E_y = f_{E_y,1} + f_{E_y,2}$, define $z = \lambda c f_{E_y,1} - \lambda c f_{E_y,2}$, then Eq.(26) + Eq.(27) and (Eq.(26) - Eq.(27)) $\times \lambda c$ give the following equations,

$$\frac{\partial E_y}{\partial t} - \frac{\partial z}{\partial x} = 0, \quad \frac{\partial z}{\partial t} - \lambda^2 c^2 \frac{\partial E_y}{\partial x} = \frac{c^2 B_z - z}{\tau}. \quad (28)$$

Expand

$$z = z_0 + \tau z_1 + \mathcal{O}(\tau^2).$$

Substitute the above expansion into Eq.(28), for $\mathcal{O}(1)$ balance, we have

$$z_0 = c^2 B_z.$$

For $\mathcal{O}(\tau)$ balance, we have

$$z_1 = -\frac{\partial z_0}{\partial t} + \lambda^2 c^2 \frac{\partial E_y}{\partial x} = \lambda^2 c^2 \frac{\partial E_y}{\partial x} - \frac{\partial c^2 B_z}{\partial t} = (\lambda^2 - 1) c^2 \frac{\partial E_y}{\partial x}.$$

Therefore, the first order approximation is $z = c^2 B_z - \tau(\lambda^2 - 1) c^2 \frac{\partial E_y}{\partial x} + \mathcal{O}(\tau^2)$, and the macroscopic equation of E_y becomes

$$\frac{\partial E_y}{\partial t} + \frac{\partial c^2 B_z}{\partial x} = \tau \frac{\partial}{\partial x} \left((\lambda^2 - 1) c^2 \frac{\partial E_y}{\partial x} \right).$$

Note that $\lambda > c$ is required for the kinetic approximation to be dissipative, which is referred to as the sub-characteristic condition by Liu [40]. This condition ensures that the relaxation system remains stable and dissipative. If $\tau = 0$ or $\lambda = 1$, the dissipation term vanishes, and the system theoretically recovers the original Maxwell equations accurately. However, even in this case, numerical dissipation will still be present in the computational results.

Next, we analyze the numerical error following the analysis in [42]. The first step is relaxation step,

$$f_{E_y,k}^*(x_i, t) = (1 - \omega) f_{E_y,k}(x_i, t) + \omega g_{E_y,k}(x_i, t), \quad (29)$$

then the second step is transport, for the sake of simplicity, we suppose this step is accurate, i.e.

$$f_{E_y,k}(x_i, t + \Delta t) = f_{E_y,k}^*(x_i - v_k \Delta t, t). \quad (30)$$

Expand Eq.(30) with respect to Δt ,

$$f_{E_y,k} + \frac{\partial f_{E_y,k}}{\partial t} \Delta t + \frac{1}{2} \frac{\partial^2 f_{E_y,k}}{\partial t^2} \Delta t^2 = f_{E_y,k}^* - \frac{\partial f_{E_y,k}^*}{\partial x} v_k \Delta t + \frac{1}{2} \frac{\partial^2 f_{E_y,k}^*}{\partial x^2} v_k^2 \Delta t^2 + \mathcal{O}(\Delta t^3). \quad (31)$$

Take the zeroth order moment, we have

$$E_y + \frac{\partial E_y}{\partial t} \Delta t + \frac{1}{2} \frac{\partial^2 E_y}{\partial t^2} \Delta t^2 = E_y^* - \frac{\partial z^*}{\partial x} \Delta t + \frac{1}{2} \frac{\partial^2 E_y^*}{\partial x^2} \lambda^2 c^2 \Delta t^2 + \mathcal{O}(\Delta t^3). \quad (32)$$

Take the first order moment, we have

$$z + \frac{\partial z}{\partial t} \Delta t + \frac{1}{2} \frac{\partial^2 z}{\partial t^2} \Delta t^2 = z^* - \frac{\partial E_y^*}{\partial x} \lambda^2 c^2 \Delta t + \frac{1}{2} \frac{\partial^2 z^*}{\partial x^2} \lambda^2 c^2 \Delta t^2 + \mathcal{O}(\Delta t^3). \quad (33)$$

For $\mathcal{O}(\Delta t)$ order of accuracy, Eq.(32) gives $E_y = E_y^*$ which is obvious since the relaxation process (29) doesn't change E_y . Eq.(33) gives $z = z^* + \mathcal{O}(\Delta t)$. Note that the first order moment of Eq.(29) gives

$$z^* = (1 - \omega)z + \omega c^2 B_z, \quad (34)$$

therefore

$$z = c^2 B_z + \mathcal{O}(\Delta t), \quad z^* = c^2 B_z + \mathcal{O}(\Delta t).$$

For $\mathcal{O}(\Delta t^2)$ order of accuracy, combining with the above formula, Eq.(32) gives

$$\frac{\partial E_y}{\partial t} + \frac{\partial c^2 B_z}{\partial x} = \mathcal{O}(\Delta t).$$

Eq.(33) gives

$$z - z^* = -\left(\frac{\partial B_z}{\partial t} + \lambda^2 \frac{\partial E_y}{\partial x}\right)c^2 \Delta t + \mathcal{O}(\Delta t^2) \equiv -\theta \Delta t + \mathcal{O}(\Delta t^2),$$

where $\theta \equiv \left(\frac{\partial B_z}{\partial t} + \lambda^2 \frac{\partial E_y}{\partial x}\right)c^2$. Substitute Eq.(34) into the above equation, we have

$$z = c^2 B_z - \frac{\theta \Delta t}{\omega t} + \mathcal{O}(\Delta t^2), \quad z^* = c^2 B_z - \frac{1 - \omega}{\omega} \theta \Delta t + \mathcal{O}(\Delta t^2). \quad (35)$$

For $\mathcal{O}(\Delta t^3)$ order of accuracy, Eq.(32) gives

$$\begin{aligned} \frac{\partial E_y}{\partial t} + \frac{\partial c^2 B_z}{\partial x} &= \left(\frac{1}{2} \frac{\partial^2 E_y}{\partial x^2} \lambda^2 c^2 - \frac{1}{2} \frac{\partial^2 E_y}{\partial t^2} + \frac{1 - \omega}{\omega} \theta\right) \Delta t + \mathcal{O}(\Delta t^2) \\ &= \left(\frac{1}{2} + \frac{1 - \omega}{\omega}\right) \theta \Delta t + \mathcal{O}(\Delta t^2). \end{aligned} \quad (36)$$

Eq.(36) gives equivalent equation to $\mathcal{O}(\Delta t^2)$. When $\omega = 2$, the $\mathcal{O}(\Delta t)$ term vanishes, resulting in a scheme of second-order temporal accuracy. It is worth noting that the above analysis is based on the assumption that the transport step is accurately solved in a Lagrangian formulation. In practice, if a finite volume method is used to solve the transport equation, numerical errors will be introduced in this step. Consequently, even with $\omega = 2$, the overall temporal accuracy may not strictly achieve second order accuracy. Therefore, it is meaningful to improve the accuracy of the transport equation.

Another way to analyze the asymptotic behavior of the scheme is from a physical perspective [43]. In this approach, the effective relaxation time associating with the numerical discretization is calculated for both the collision and transport steps. For the collision step, the overall dissipation decreases, while for the transport step, the overall dissipation increases. This analysis provides a method to better understand the relation between microscopic mean relaxation time τ and macroscopic dissipation parameters, such as the viscosity coefficient, for the splitting scheme like Lattice Boltzmann Method (LBM), and Discrete Unified Gas-Kinetic Scheme (DUGKS) [43].

6. Numerical tests

6.1. Plane wave test

In this section, we utilize the plane wave solution of Maxwell's equations to evaluate the convergence order of the algorithm. We then compare the runtime of the Beam-ET method

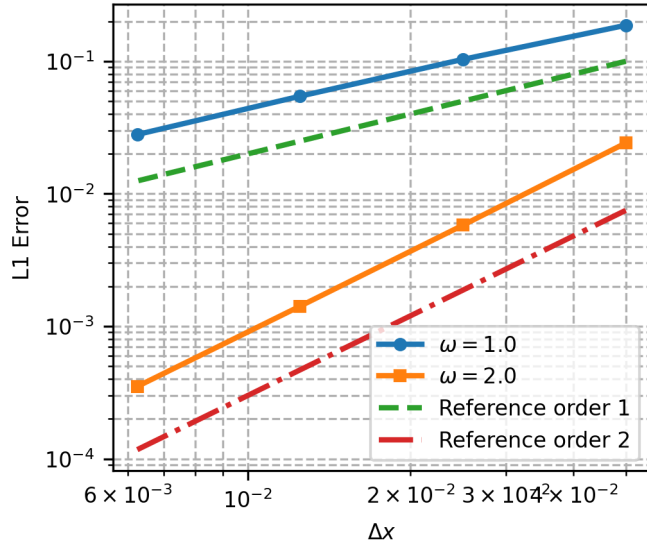


Figure 2: Accuracy test: L^1 error of the 3D polarized Maxwell equation of $\omega = 1.0$ and $\omega = 2.0$.

and the FDTD method in a three-dimensional context using this test case. The spatial domain is defined as $x \in [0, 1]$ and $t_{max} = 1.0$. We use the following exact time-domain solution for a plane wave:

$$\begin{cases} E_z(\mathbf{x}, t) = \cos(2\pi(x - ct)), \\ B_y(\mathbf{x}, t) = -\cos(2\pi(x - ct)). \end{cases} \quad (37)$$

The timestep is set as $\Delta t = \Delta x / (\lambda c)$ so as to ensure the accuracy in the transport step. Mesh number $N = 20^3, 40^3, 80^3, 160^3$ is used. The boundary condition is periodic to eliminate the influence of the boundary. From Figure 2, we can see that the order of accuracy is second-order when $\omega = 2.0$ and first-order when $\omega = 1.0$. This result is consistent with the asymptotic analysis in Section 5.

The runtime of the Beam-ET method and the FDTD method in the three-dimensional case is compared next. The implementation of the FDTD method follows the approach described in [44]. The test case is the same as the accuracy test, with mesh sizes ranging from 40^3 to 200^3 . As the mesh size increases, the runtime of the Beam-ET method is approximately three times that of the FDTD method. The exact runtime of the Beam-ET method and the FDTD method is shown in Table 2. It is reasonable that the Beam-ET method is slower than the FDTD method because it requires more computational resources to solve the kinetic equation. In the three-dimensional case, the Beam-ET method has to solve four times as many equations as the FDTD method, since for each macroscopic variable, there are four microscopic kinetic velocities.

6.2. Rectangular current density pulse test

In this section, we consider a rectangular current density pulse test case to demonstrate the multidimensional capabilities of our method. We also discuss the comparison with the FDTD method in the presence of discontinuities. First, we utilize the Beam-ET and Beam-CTU methods to compare with FVS scheme, as the former two methods exhibit multidimensionality

Table 2: Runtime comparison between FDTD and Kinetic Parallel methods for different mesh sizes.

Mesh Size	Runtime FDTD(s)	Runtime Beam-ET(s)	Runtime Ratio
40^3	0.1005	0.5912	5.88
60^3	0.6071	2.5763	4.24
80^3	2.9021	8.7799	3.03
100^3	8.2269	27.1414	3.30
120^3	17.6980	59.6590	3.37
140^3	34.0475	112.1295	3.29
160^3	63.8085	193.3380	3.03
180^3	109.2115	302.8429	2.77
200^3	163.4793	472.2845	2.89

while the latter does not. This multidimensionality allows for higher CFL numbers, resulting in greater accuracy with fewer mesh elements. Next, we compare the Beam-ET method with the FDTD method, noting that the FDTD method experiences oscillations following discontinuities, while the Beam-ET method can mitigate these oscillations by adjusting the relaxation parameter ω .

Define a square-shaped current density pulse $\mathbf{J} = J_z \hat{e}_z \equiv \sigma E_z \hat{e}_z$ centered within the computational domain $\Omega = [0, 1] \times [0, 1]$ as follows:

$$E_z = F(\mathbf{x}), \quad \mathbf{x} \in \Omega, \quad (38)$$

where $\sigma = 1.0$ is the electric conductivity. The function $F(\mathbf{x}) \equiv F(x, y)$ is defined as:

$$F(x, y) = [H(x - x_1) - H(x - x_2)] \cdot [H(y - y_1) - H(y - y_2)].$$

Here, $H(x)$ represents the Heaviside function, and the parameters are set as $x_1 = y_1 = 0.25$ and $x_2 = y_2 = 0.75$. The setting is shown in Figure 3, when a current pulse \mathbf{J} in the \hat{e}_z is initially applied in the \hat{e}_z direction within the gray rectangular region, it generates magnetic field \mathbf{B} in the xy-plane. This change in magnetic flux subsequently induces an electric field \mathbf{E} , which then propagates throughout the computational domain.

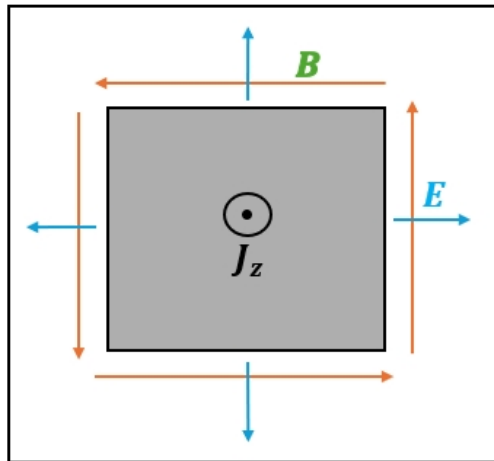


Figure 3: Demonstration of the induced magnetic field and electromagnetic field following the application of a current pulse.

The CFL number is defined by

$$CFL = \max\left(\frac{u\Delta t}{\Delta x}, \frac{v\Delta t}{\Delta y}, \frac{w\Delta t}{\Delta z}\right),$$

where u, v, w is the microscopic velocity in x, y, z direction, respectively.

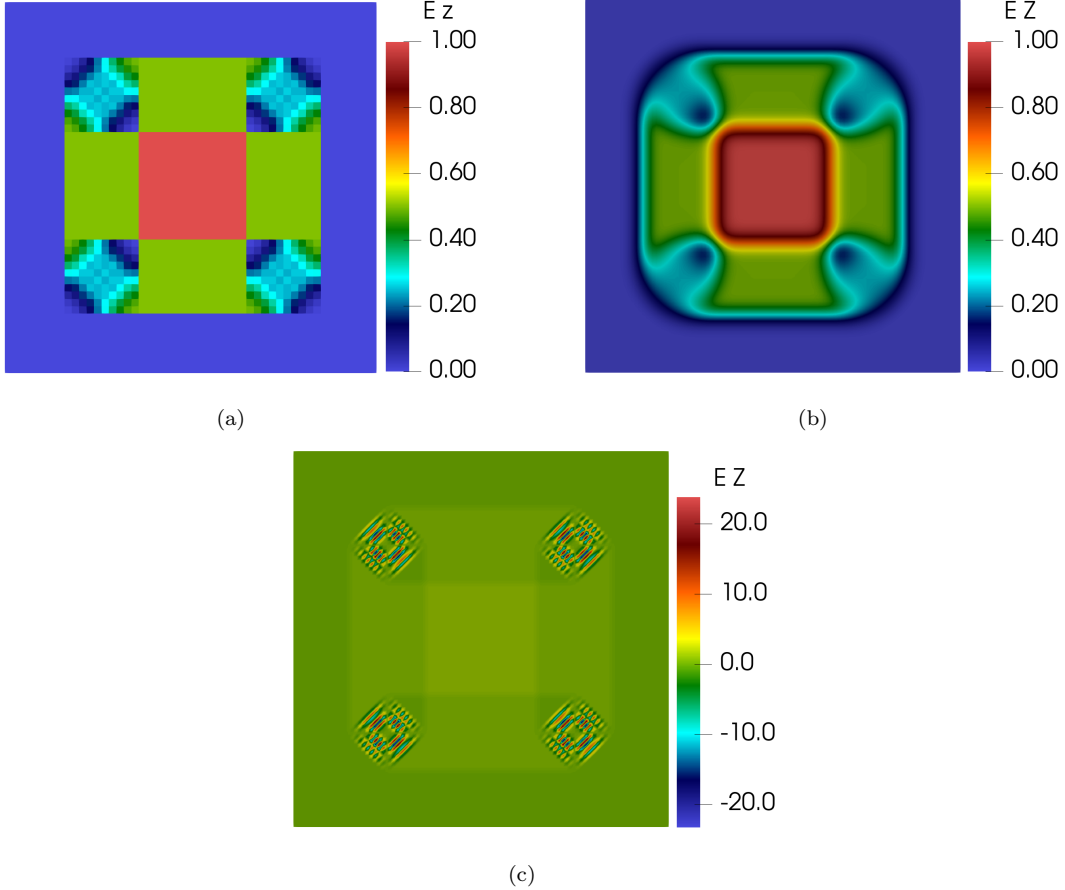


Figure 4: Rectangular current response. (a) E_z profile by Beam-ET with $N = 100$ and $CFL=1.0$, (b) E_z profile by FVS with $N = 100$ and $CFL=0.5$, (c) E_z profile by FVS with $N = 100$ with $CFL=1.0$. The Beam-ET method accurately captures the electric evolution after the current density pulse while the results by the FVS method are less accurate due to a maximum CFL number of 0.5. When we increase the CFL number to 1.0, the FVS method becomes unstable.

Figure 4 presents the results of the rectangular current density pulse simulation, with the electric field E_z plotted at $t = 0.1$ for both the Beam-ET and FVS methods. The Beam-ET method accurately captures the electric evolution after the current density pulse, as illustrated in Figure 4(a). In contrast, the results by the FVS method are less accurate due to a maximum CFL number of 0.5, as shown in Figure 4(b). When we increase the CFL number to 1.0, the results by the FVS method become unstable, as depicted in Figure 4(c). To achieve accuracy comparable to that of the Beam-ET method, the FVS method requires denser meshes. As the mesh is refined, the FVS results gradually converge towards those of the Beam-ET and Beam-CTU method, as demonstrated in Figure 5. The multidimensional property enables higher Courant numbers and saves computational resources by reducing the number of mesh cells needed to achieve similar accuracy.

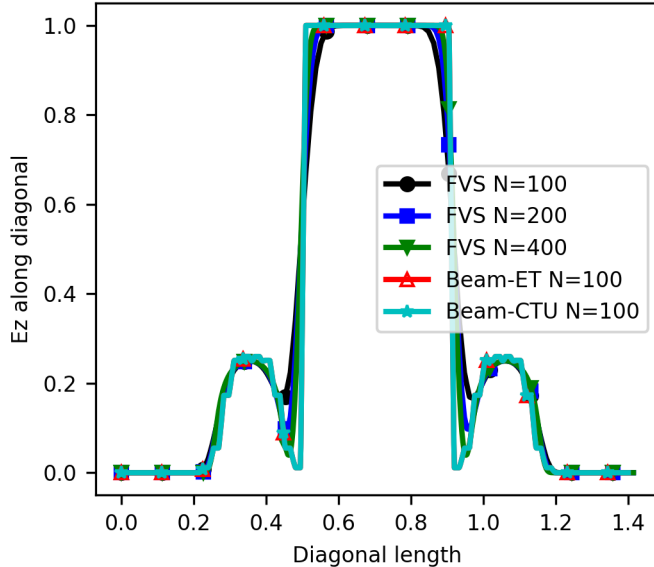


Figure 5: Comparison of E_z along the diagonal line $x = y = z$ at $t = 0.1$. As the mesh is refined, the FVS results gradually converge toward those of the Beam-ET and Beam-CTU methods.

Next, we examine the results of the FDTD method, as shown in Figure 6. We find that under initial conditions with discontinuities, the FDTD method produces oscillations near these discontinuities, which may be caused by dispersion errors, requiring further investigation. For the Beam-ET method, if we set $\omega = 1.0$, the Beam-ET method gives stable results, while if we set $\omega = 2.0$, the Beam-ET method also generates oscillating results. To suppress the oscillations, we need to adjust the relaxation parameter ω locally based on the smoothness of the local field. A straightforward strategy is to set $\omega = 1.0$ near the discontinuities and $\omega = 2.0$ elsewhere. To measure the smoothness of field f at cell i , a smoothness detector based on the idea of van Leer limiter is constructor as follows:

$$\omega_i = \begin{cases} 1, & \text{if } L(s_{i+}, s_{i-}) = 0 \text{ or } > s_{max}, \\ 2, & \text{else} \end{cases} \quad (39)$$

where $s_{i+} = (f_{i+1} - f_i)/\Delta x$, $s_{i-} = (f_i - f_{i-1})/\Delta x$ and

$$L(s_{i+}, s_{i-}) = (\text{sign}(s_{i+}) + \text{sign}(s_{i-})) \frac{2|s_{i+}||s_{i-}|}{|s_{i+}| + |s_{i-}|},$$

where s_{max} is a maximum allowed slope. Here is the idea of the detector. If $L(s_{i+}, s_{i-}) = 0$, it indicates that the field has no gradient or exhibits oscillations, both of which are suitable for setting $\omega = 1.0$. In the case of no gradient, there will be no dynamic evolution, so temporal accuracy doesn't matter. If oscillations are present, reducing the temporal accuracy to first order can help stabilize the results. Conversely, if $L(s_{i+}, s_{i-}) > s_{max}$, the slope becomes significantly large, indicating that the field is not smooth, requiring a reduction in temporal accuracy to stabilize the results. For other cases, using $\omega = 2.0$ for second-order temporal accuracy is appropriate. The results of different s_{max} are shown in Figure 7. The results show that the suppression strategy effectively mitigates the oscillations near the discontinuities. And as s_{max} decreases, the oscillations are effectively suppressed.

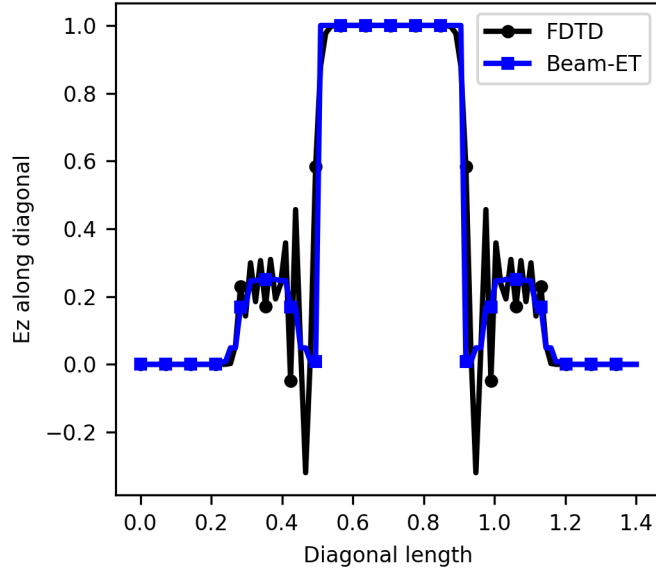


Figure 6: Comparison of E_z along the diagonal line $x = y = z$ at $t = 0.1$. As shown in the figure, the FDTD method generates oscillations near the discontinuities, while the Beam-ET does not.

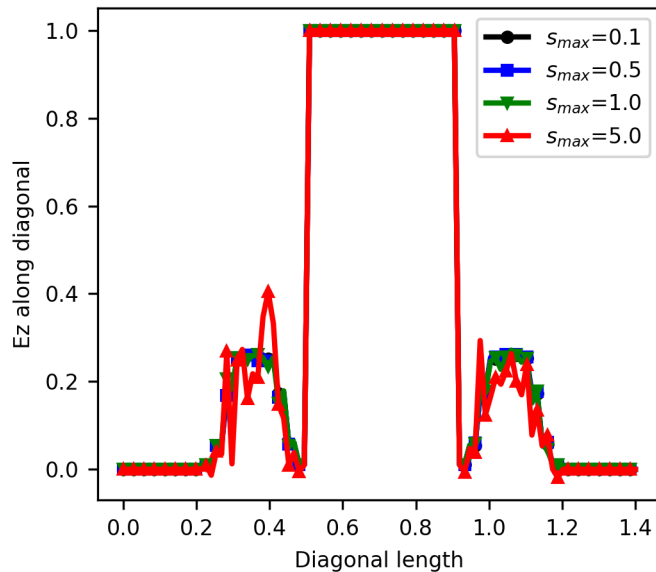


Figure 7: Comparison of E_z along the diagonal line $x = y = z$ at $t = 0.1$ with different s_{max} in the smoothness detector. The results show that the suppression strategy effectively mitigates the oscillations near the discontinuities. And as the s_{max} decreases, the oscillations are more effectively suppressed.

6.3. Antenna simulation

In this section, we consider the case of a plane wave interacting with a conductive antenna placed in a vacuum to test the coupling of the source term. The antenna has a length of 0.25 and a diameter of 0.05, and it is oriented along the z -axis within the computational domain defined as $\mathcal{D} = [0, 1]^3$. The mesh is coarse in the vacuum region while being refined around the antenna, as illustrated in Figure 8. The conductivity of the antenna is represented by $\sigma \neq 0$,

indicating that it can conduct electricity, whereas the vacuum surrounding the antenna has a conductivity of $\sigma = 0$, signifying that it is an insulator.

The incident plane wave is an exact solution of Maxwell's equations without source term

$$\begin{cases} E_z(\mathbf{x}, t) = f(y - y_0 - t), \\ B_x(\mathbf{x}, t) = f(y - y_0 - t), \end{cases} \quad (40)$$

where f is the following compactly supported function[21](i.e. bump function):

$$f(x) = \begin{cases} \exp\left(1 - \frac{1}{1 - \frac{|x|}{\eta}}\right) & \text{if } |x| < \eta \\ 0 & \text{otherwise} \end{cases}$$

with $\eta = 0.25$ representing the diameter of the bump and $y_0 = 0.45$ the initial center location of the bump. The total simulation time is set to $t_{total} = 0.1$, during which the plane wave propagates in the y direction, sweeping its peak location across the antenna. Several behaviors are expected to be observed throughout this process. Firstly, The electric field component E_z will induce a current J_z within the antenna. Secondly, the induced current J_z will then generate magnetic fields B_x and B_y around the antenna. Thirdly, at both the upper and lower ends of the antenna, the condition $\nabla \cdot \mathbf{J} \neq 0$ indicates that there will be an accumulation of electric charges. This accumulation leads to the formation of an electric field at these locations.

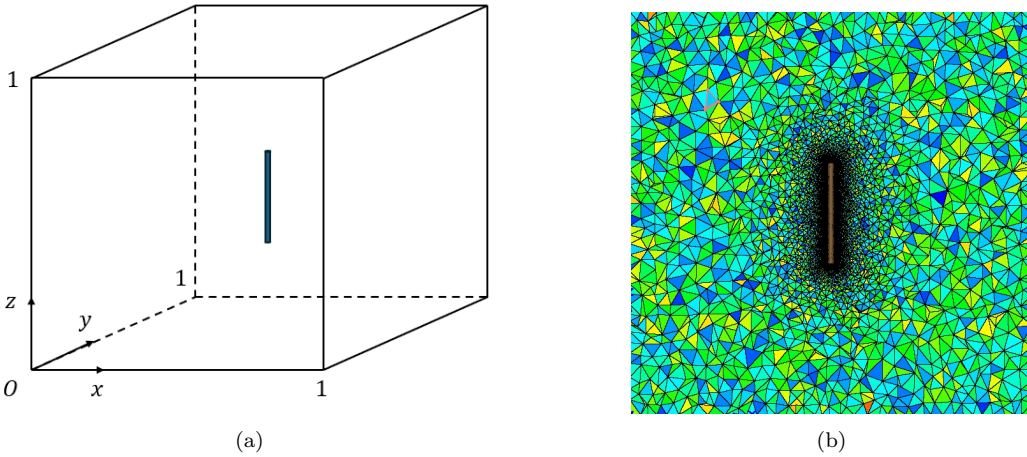


Figure 8: Antenna simulation: (a) schematic of the computational domain and geometry setting, (b) sliced mesh at $x = 0.5$.

The conductivity of the antenna is set to $\sigma = 2 \times 10^4$. Figure 9 illustrates the contours of E_y and B_y at $t = 0.05$ seconds. In Figure 9(a), the electric field induced by the accumulated charges at the ends of the antenna is observed. This phenomenon is consistent with the expected behavior of charge separation in a conductive antenna exposed to an electromagnetic wave. Figure 9(b) demonstrates the magnetic field generated around the antenna due to the induced current. At $t = 0.1$, the peak of the plane wave has moved past the antenna to its right side, as depicted in Figure 10. At this point, the accumulated charges begin to neutralize and the magnetic field around the antenna approaches equilibrium as the wave passes.

In Figure 11, we present a detailed comparison of the kinetic scheme and the referenced upwind scheme, focusing on the profiles of E_y and B_y along specific lines. Figure 11(a) displays

the exact profile of E_y along the line $z = 0.625$. The results demonstrate good agreement between the kinetic scheme and the referenced scheme. Figure 11(b) illustrates the exact profile of B_y along the line $z = 0.5$. In this case, both methods show good concordance.

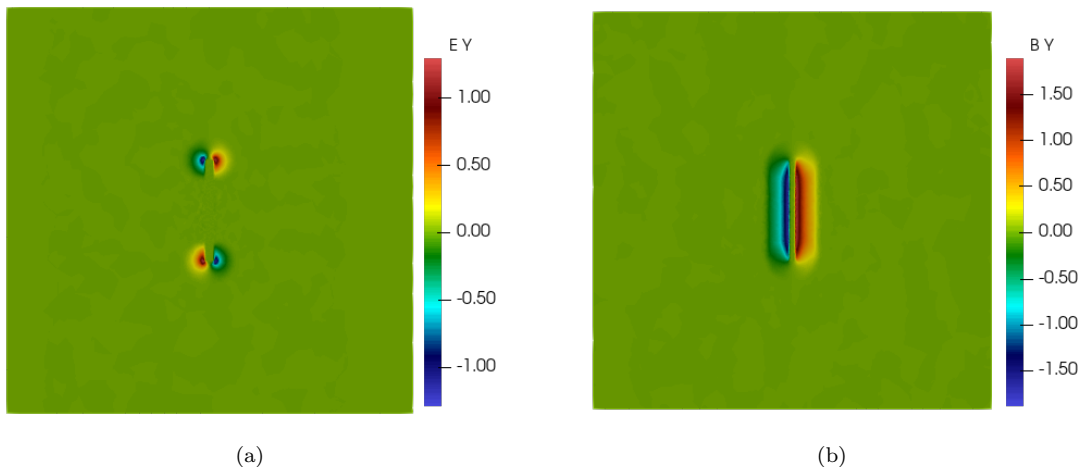


Figure 9: Antenna simulation: (a) E_y (b) B_y at $t = 0.05$. The electric field induced by the accumulated charges at the ends of the antenna is observed. The magnetic field generated around the antenna due to the induced current is also observed.

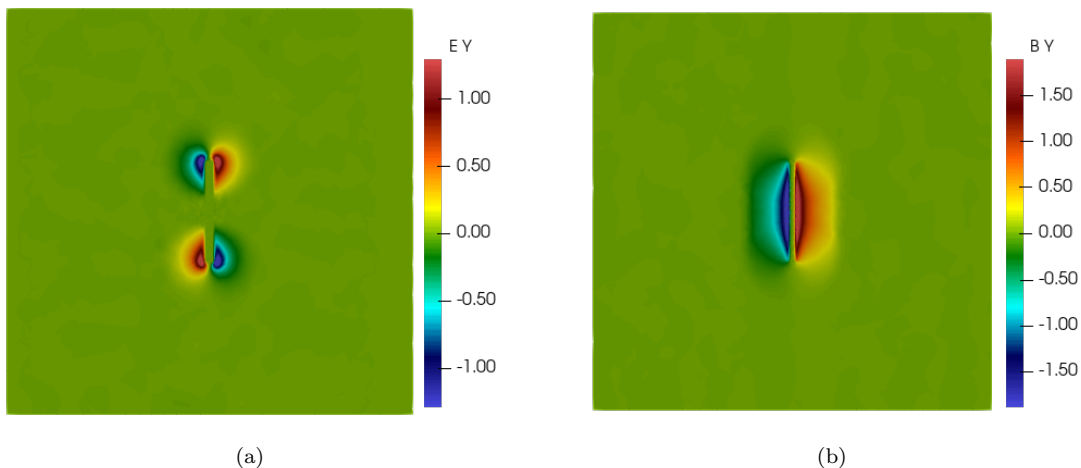


Figure 10: Antenna simulation: (a) E_y (b) B_y at $t = 0.1$. the peak of the plane wave has moved past the antenna to its right side, the accumulated charges begin to neutralize and the magnetic field around the antenna approaches equilibrium as the wave passes.

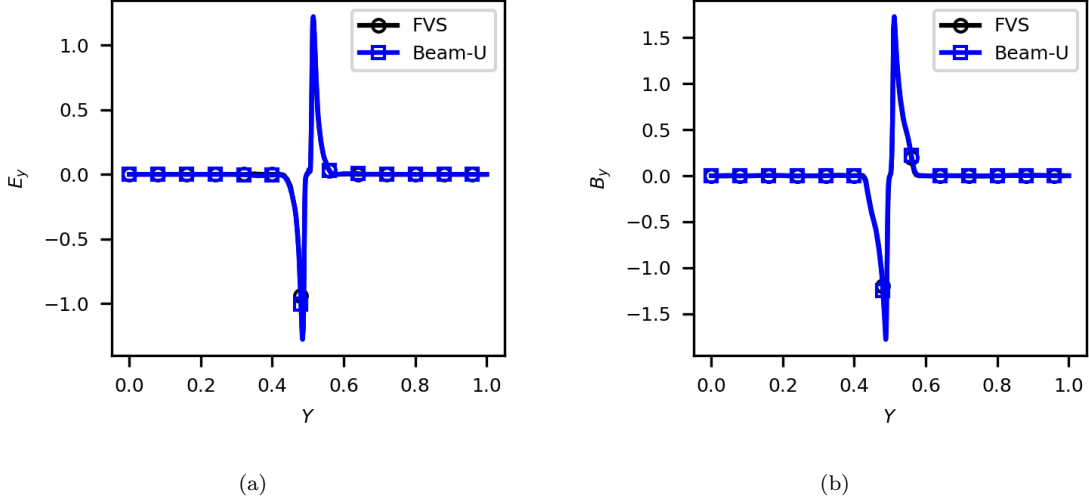


Figure 11: Antenna simulation: (a) E_y (b) B_y at $t = 0.05$. The results demonstrate good agreement between the kinetic scheme and the referenced FVS scheme.

6.4. Sphere scattering test

In this section, we examine the scattering of a plane wave by a sphere to evaluate the method's performance on unstructured meshes. When the wavelength of the incident wave is significantly larger than the sphere's diameter, Rayleigh scattering occurs. In this regime, the scattering intensity is inversely proportional to the fourth power of the wavelength. Conversely, as the wavelength approaches the sphere's diameter, Mie scattering takes place where a greater proportion of the scattered power is scattered forward. For Rayleigh scattering, the quasi-static approximation is valid in the near field of the scatterer. However, for Mie scattering, the quasi-static approximation is not applicable, and the full wave equation must be solved. This test case is used to evaluate the method's accuracy on the unstructured mesh. The geometry and mesh setting is shown in Figure 12. The sphere's surface is perfectly conducting, with a radius of $R = 1$. The computational domain is $[-5, 5] \times [-5, 5] \times [-5, 5]$. The mesh is tetrahedral and locally refined around the sphere. The number of tetrahedral cells is 2390968.

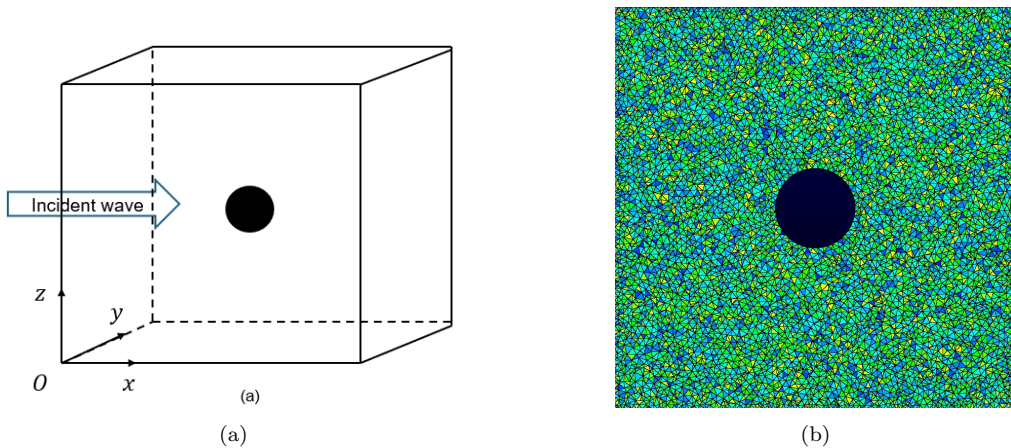


Figure 12: Sphere scattering simulation: (a) schematic of the computational domain and geometry setting, (b) sliced mesh at $x = 0.5$.

The incident plane wave traveling at the $+x$ direction is given as follows:

$$\begin{cases} \mathbf{E}_{inc}(\mathbf{x}, t) = \cos(\pi(x - ct))\hat{e}_z, \\ \mathbf{B}_{inc}(\mathbf{x}, t) = -\cos(\pi(x - ct))\hat{e}_y. \end{cases} \quad (41)$$

The wavelength of the incident plane wave is 2, which is equal to the diameter of the sphere. On the surface of the sphere, the following boundary condition is applied:

$$\begin{cases} \mathbf{n} \times (\mathbf{E}_1 - \mathbf{E}_2) = 0, \\ \mathbf{n} \times (\mathbf{H}_1 - \mathbf{H}_2) = \mathbf{J}_s, \\ \mathbf{n} \cdot (\mathbf{B}_1 - \mathbf{B}_2) = 0, \\ \mathbf{n} \cdot (\mathbf{E}_1 - \mathbf{E}_2) = \rho_s/\epsilon, \end{cases} \quad (42)$$

where \mathbf{n} is the normal vector of the surface, \mathbf{J}_s is the surface current density, ρ_s is the surface charge density. The subscripts 1 and 2 represent the values on the two sides of the surface. On a perfectly conducting surface, the tangential electric field and the normal magnetic field are zero. The unknown surface current and charge densities are treated as jumps across the surface [45], then we have the following conditions:

$$\begin{cases} \mathbf{n} \cdot \nabla(\mathbf{n} \times (\mathbf{H}_1 - \mathbf{H}_2)) = \mathbf{n} \cdot \nabla \mathbf{J}_s = 0, \\ \mathbf{n} \cdot \nabla(\mathbf{n} \cdot (\mathbf{D}_1 - \mathbf{D}_2)) = \mathbf{n} \cdot \nabla(\rho_s/\epsilon) = 0. \end{cases} \quad (43)$$

This turns out to be a Neumann boundary condition for the normal electric field and the tangential magnetic field. For the outer boundary, an absorbing boundary condition such as the Perfect Matched Layer (PML) should be applied. However, for simplicity, the analytical solution of the incident wave is applied, and works relatively well in this case.

The results are shown in Figure 13. Figure 13(a) shows the total E_z field at $t = 10$. The scattered field of E_z is shown in Figure 13(b). The scattered field is calculated by subtracting the incident field from the total field, i.e.

$$\mathbf{E}_s = \mathbf{E}_{total} - \mathbf{E}_{incident}.$$

The forward scattering feature of the Mie scattering is captured as shown in Figure 13(b). The total electric field profile around the circle of radius $1.5R$ on the xy -plane at $z = 0.5$ is shown in Figure 12. The results agrees well with the reference solution, which is calculated by the FVS method directly.

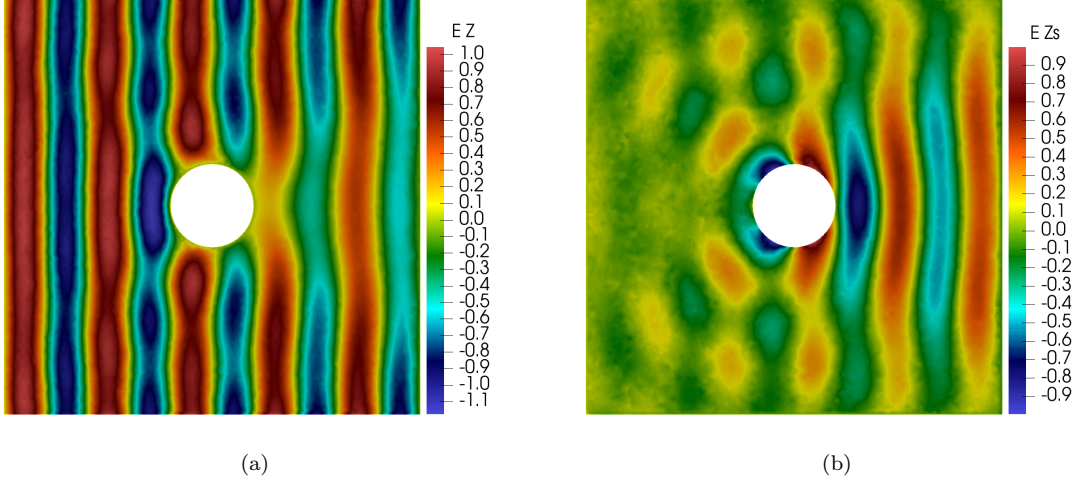


Figure 13: Sphere scattering simulation: (a) E_z contour (b) Scatter field E_z contour at $t = 10$. The forward scattering feature of the Mie scattering is captured

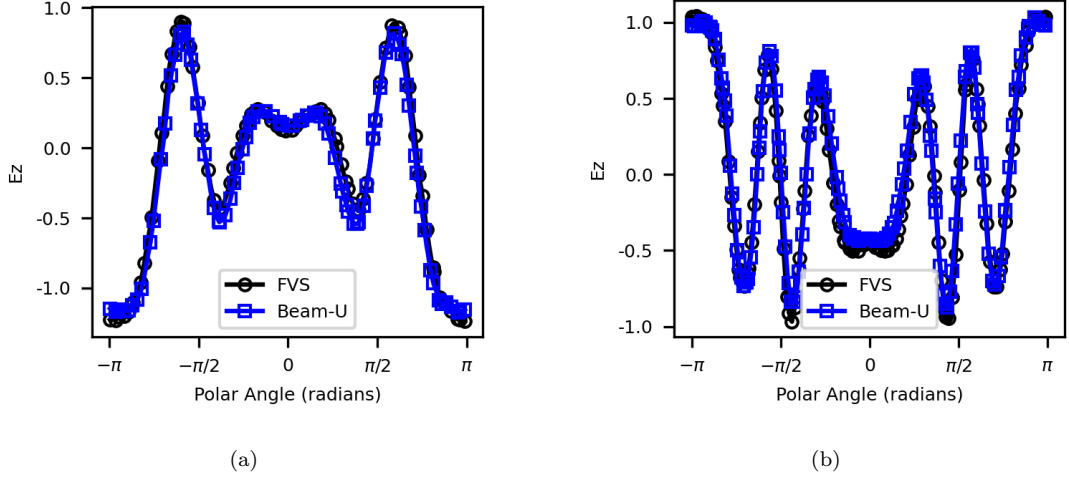


Figure 14: Comparison between FVS and Beam-U method on a circle with radius (a) 1.5, (b) 2.5. The results agrees well with the reference solution, which is calculated by the FVS method directly.

6.5. Flight vehicle scattering test

In this section, we consider a more complex geometric shape, i.e. flight vehicle to further test the performance on the unstructured mesh. The incident wave coming in the $+x$ direction is given as follows:

$$\begin{cases} \mathbf{E}_{inc}(\mathbf{x}, t) = \sin(k\pi(x - ct))\hat{e}_z, \\ \mathbf{B}_{inc}(\mathbf{x}, t) = -\sin(k\pi(x - ct))\hat{e}_y. \end{cases} \quad (44)$$

where $c = 1, k = 0.005$. The computational domain size is $[L_x, L_y, L_z] = [1500, 900, 800]$, where L_x, L_y, L_z is the computational domain length along x, y, z direction. The spatial size of the vehicle is around $[l_x, l_y, l_z] = [310, 80, 160]$, where l_x, l_y, l_z is the characteristic length of the vehicle along different directions. The mesh is mixed tetrahedral and hexahedron and locally refined around the flight vehicle. The number of total cells is 1710906. The geometry and mesh setting is shown in Figure 15. The surface of the vehicle is treated as PEC.

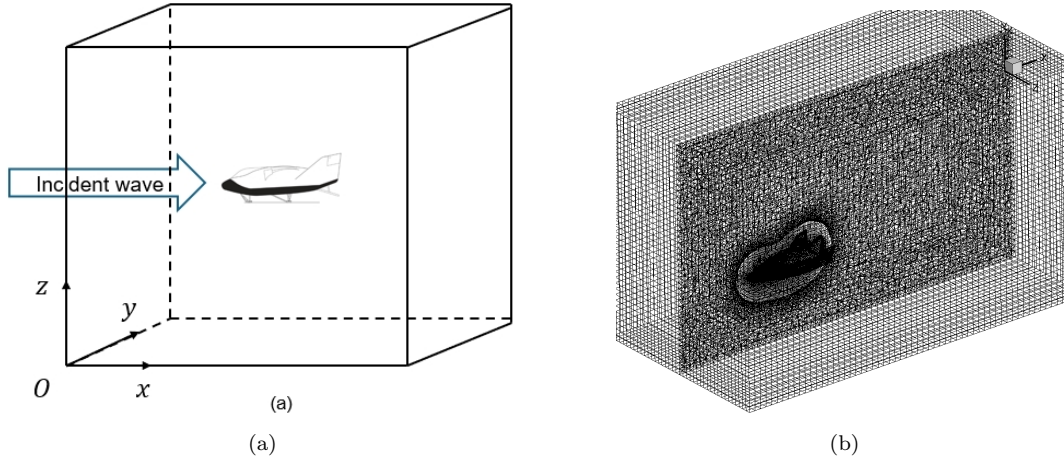
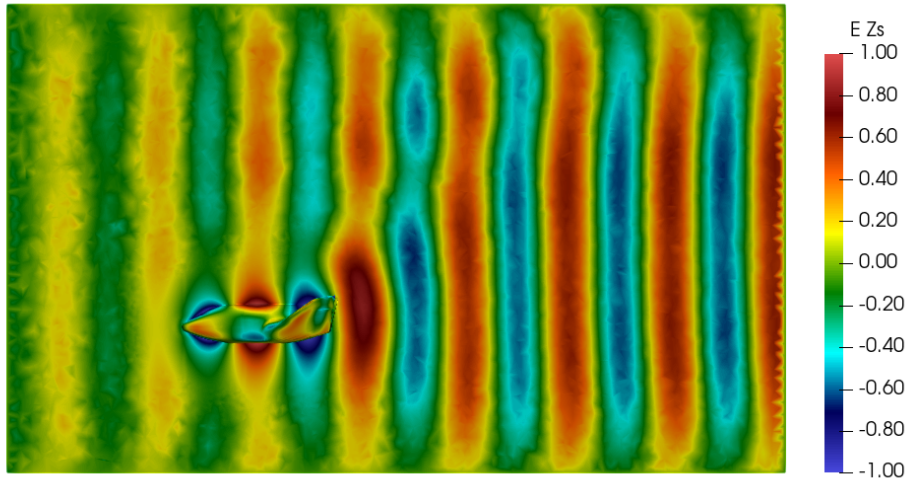
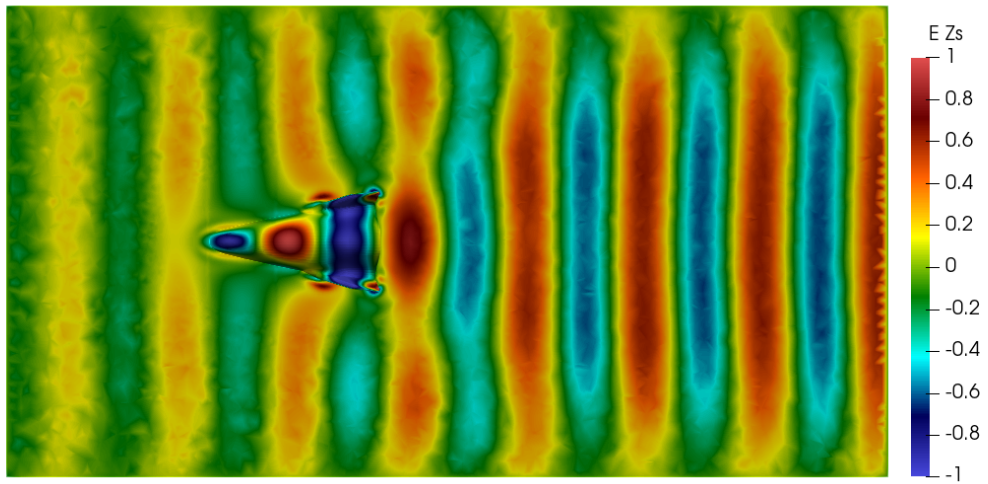


Figure 15: Flight vehicle scattering simulation: (a) schematic of the computational domain and geometry setting, (b) mesh setting, The mesh is refined around the flight vehicle.

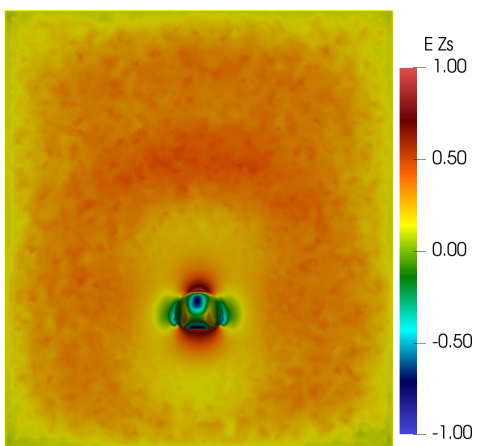
The scattered field E_{zs} is shown in Figure 16. In the Figure 16 (a), the scattered field E_{zs} at $z = 0$ plane is shown. In the Figure 16 (b), the scattered field E_{zs} at $y = 40$ plane is shown. In the Figure 16 (c) and (d), the scattered field E_{zs} at $x = 160$ and $x = 260$ plane is shown. The above figures show that scattering occurs mainly in the x-direction, indicating forward Mie scattering. This observation is expected since the wavelength of the incident wave is comparable to the size of the scatterer. Delicate structures, such as wings, exhibit more intricate scattering patterns.



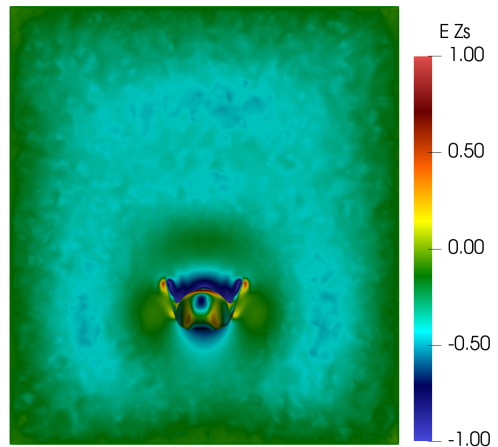
(a)



(b)



(c)



(d)

Figure 16: E_z field at different slices. (a) $z = 0$, (b) $y = 40$, (c) $x = 160$, (d) $x = 260$. The scattering occurs mainly in the x-direction, indicating forward Mie scattering.

6.6. Charge conservation test

In this section, we consider a charge conservation test to evaluate our method's capability to correct inconsistencies between charge and current distributions. Normally the divergence constraints are taken as an initial condition, suppose $\nabla \cdot \mathbf{B}|_{t=0} = 0$ and $\epsilon_0 \nabla \cdot \mathbf{E}|_{t=0} = \rho$ initially, then we have

$$\begin{aligned}\partial_t(\nabla \cdot \mathbf{B}) &= \nabla \cdot \partial_t \mathbf{B} = \nabla \cdot (-\nabla \times \mathbf{E}) = 0, \\ \partial_t(\epsilon_0 \nabla \cdot \mathbf{E} - \rho) &= \nabla \cdot \partial_t \epsilon_0 \mathbf{E} - \partial_t \rho = \nabla \cdot \mathbf{J} + \partial_t \rho \neq 0.\end{aligned}$$

In this case, the charge conservation equation (Eq.(45)) is violated, which can be used to test the algorithm's capability to correct inconsistencies between charge and current distributions,

$$\partial_t \rho + \nabla \cdot \mathbf{J} = 0. \quad (45)$$

For simplicity, we consider a two-dimensional numerical problem using Cartesian coordinates $\mathbf{x} = (x, y)^T$. We define a square-shaped charge density distribution centered within the computational domain $\Omega = [0, 1] \times [0, 1]$ as follows:

$$\rho(\mathbf{x}, t) = \rho_0 \omega t F(\mathbf{x}), \quad \mathbf{x} \in \Omega, \quad t \geq 0, \quad (46)$$

where $\rho_0 = 1.0 \times 10^{-12}$ is a constant and $\omega = 1.0$ is the frequency. The function $F(\mathbf{x}) \equiv F(x, y)$ is defined as:

$$F(x, y) = [H(x - x_1) - H(x - x_2)] \cdot [H(y - y_1) - H(y - y_2)],$$

where the parameters are set as $x_1 = y_1 = 0.49$ and $x_2 = y_2 = 0.51$. To introduce inconsistencies between charge and current, the current density is enforced to be zero, i.e.,

$$\mathbf{J}(\mathbf{x}, t) \equiv 0, \quad \mathbf{x} \in \Omega, \quad t \geq 0.$$

The electromagnetic fields are initialized as $\mathbf{E}(\mathbf{x}, t = 0) = 0$ and $\mathbf{B}(\mathbf{x}, t = 0) = 0$ for all $\mathbf{x} \in \Omega$. Under these conditions, a traditional solver that only addresses the hyperbolic part of Maxwell's equations will yield results where $\mathbf{E}(\mathbf{x}, t) = 0$ and $\mathbf{B}(\mathbf{x}, t) = 0$ at all times. However, thanks to the correction mechanism of the PHM system, the charge information is not ignored but instead transferred to the Lagrange multiplier ϕ . This approach allows the inconsistencies to be captured and propagated out of domain by ϕ at a speed of χc [17]. As a result, the PHM system effectively rebuilds the charge conservation property, making the numerical results physically reliable. Figure 17 shows the E_x and E_y field at $t = 5$. The electric monopole field pattern is correctly captured.

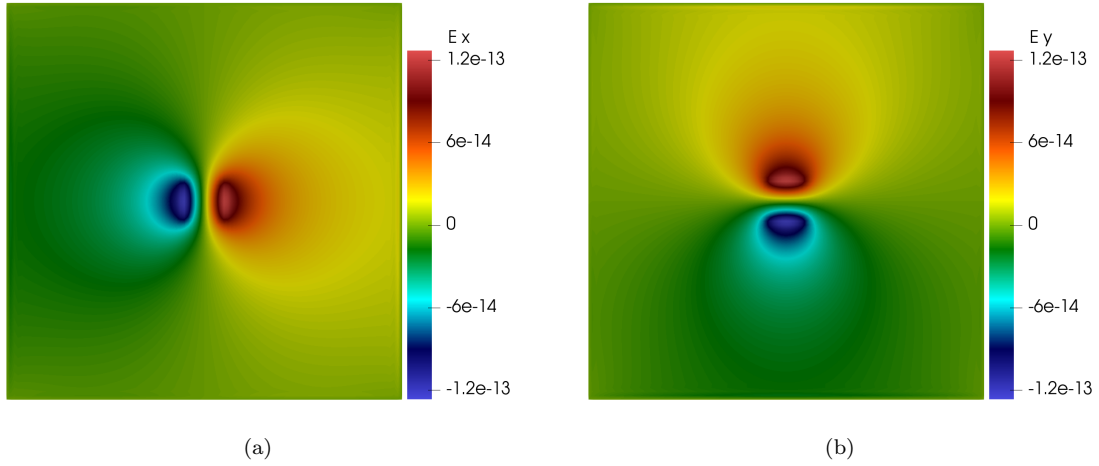


Figure 17: Charge conservation: (a) E_x (b) ϕ at $t = 5$. The electric monopole field pattern is correctly captured.

To quantify the inconsistencies between charge and current, we consider the following L_2 -norm as the measurement,

$$\frac{1}{\chi} \left\| \frac{\partial \tilde{\phi}}{\partial t} \right\|_{L_2} := \frac{1}{\chi \Delta t} \sqrt{\sum_{i=1}^N [\phi_i^{n+1} - \phi_i^n]^2} / \frac{\rho_0}{\epsilon_0},$$

where i is the index of the cell and V_i is the volume of the cell. Figure 18 demonstrates that the inconsistencies are maintained in a constant state over time, rather than increasing all the time as would be the case with a traditional Maxwell solver.

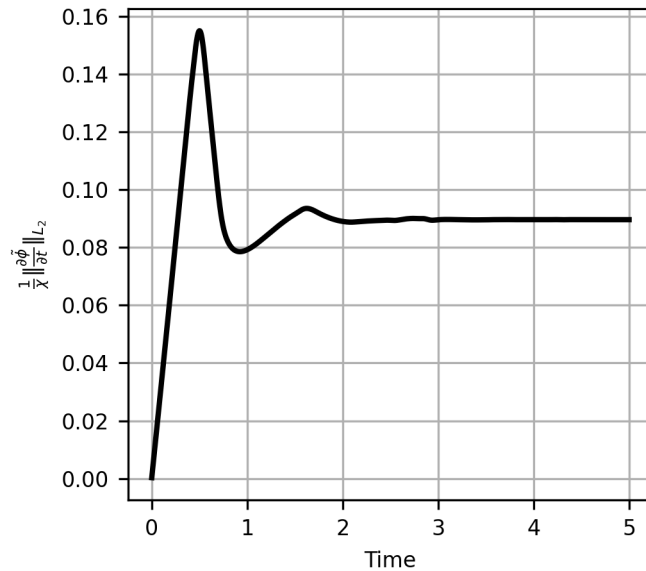


Figure 18: Evolution of inconsistencies between charges and currents. The inconsistencies are controlled in a constant state over time.

7. Conclusion

In this work, we present a gas-kinetic scheme based on discrete velocity space for solving Maxwell equations. This method achieves spatial and temporal second-order accuracy as the Finite-Difference Time-Domain (FDTD) method on structured meshes, without the need for a staggered grid and leapfrog update. This is proved in section 5 analytically through a simplified 1-D polarized Maxwell equation and in section 6.1 through 3-D numerical experiments. Besides, as shown in section 6.2, this method benefits from true multidimensionality due to its kinetic formulation and permits larger timestep in multidimensional case. This is the inherent advantage of the kinetic formulation. This method is more stable in the presence of discontinuity due to its flexibility to switch between first-order and second-order temporal order accuracy through relaxation parameters. Furthermore, the kinetic formulation is easier to be extended to unstructured meshes. A series of test cases, including the antenna simulations, the sphere scattering and the flight vehicle scattering are tested. The results match well with the Riemann-solver-based method. Finally, charge conservation capability due to the special form of the Maxwell equations is discussed through the test case.

Acknowledgements

This work was supported by the National Key R&D Program of China (Grant No. 2022YFA1004500) and the National Natural Science Foundation of China (Nos. 12172316 and 92371107), and the Hong Kong Research Grant Council (Nos. 16208021, 16301222, and 16208324).

References

- [1] A. Taflove, S. C. Hagness, M. Picket-May, Computational electromagnetics: the finite-difference time-domain method, *The Electrical Engineering Handbook 3* (629-670) (2005) 15.
- [2] K. Yee, Numerical solution of initial boundary value problems involving maxwell's equations in isotropic media, *IEEE Transactions on antennas and propagation* 14 (3) (1966) 302–307.
- [3] R. Holland, Finite-difference solution of maxwell's equations in generalized nonorthogonal coordinates, *IEEE Transactions on Nuclear Science* 30 (6) (1983) 4589–4591.
- [4] K. S. Yee, J. S. Chen, The finite-difference time-domain (FDTD) and the finite-volume time-domain (FVTD) methods in solving maxwell's equations, *IEEE Transactions on Antennas and Propagation* 45 (3) (1997) 354–363.
- [5] P. Monk, *Finite element methods for Maxwell's equations*, Oxford university press, 2003.
- [6] J.-C. Nédélec, Mixed finite elements in \mathcal{R}^3 , *Numerische Mathematik* 35 (1980) 315–341.
- [7] A. Fisher, R. N. Rieben, G. H. Rodrigue, D. A. White, A generalized mass lumping technique for vector finite-element solutions of the time-dependent maxwell equations, *IEEE transactions on antennas and propagation* 53 (9) (2005) 2900–2910.
- [8] R. F. Harrington, *Field computation by moment methods*, Krieger Publishing Co., Inc., 1982.

- [9] A. Bondeson, T. Rylander, P. Ingelström, Computational electromagnetics, Springer, 2012.
- [10] P. Monk, Y. Zhang, Finite element methods for maxwell’s equations (2019). [arXiv: 1910.10069](https://arxiv.org/abs/1910.10069).
- [11] A. Jameson, W. Schmidt, E. Turkel, Numerical solution of the euler equations by finite volume methods using runge kutta time stepping schemes, in: 14th fluid and plasma dynamics conference, 1981, p. 1259.
- [12] R. J. LeVeque, Finite volume methods for hyperbolic problems, Vol. 31, Cambridge university press, 2002.
- [13] E. F. Toro, Riemann solvers and numerical methods for fluid dynamics: a practical introduction, Springer Science & Business Media, 2013.
- [14] A. H. Mohammadian, V. Shankar, W. F. Hall, Computation of electromagnetic scattering and radiation using a time-domain finite-volume discretization procedure, Computer Physics Communications 68 (1-3) (1991) 175–196.
- [15] J. S. Shang, D. Gaitonde, Characteristic-based, time-dependent maxwell equation solvers on a general curvilinear frame, AIAA journal 33 (3) (1995) 491–498.
- [16] C.-D. Munz, P. Omnes, R. Schneider, E. Sonnendrücker, U. Voss, Divergence correction techniques for maxwell solvers based on a hyperbolic model, Journal of Computational Physics 161 (2) (2000) 484–511.
- [17] C.-D. Munz, P. Ommes, R. Schneider, A three-dimensional finite-volume solver for the maxwell equations with divergence cleaning on unstructured meshes, Computer Physics Communications 130 (1-2) (2000) 83–117.
- [18] C.-D. Munz, R. Schneider, U. Voß, A finite-volume method for the maxwell equations in the time domain, SIAM Journal on Scientific Computing 22 (2) (2000) 449–475.
- [19] A. Taube, M. Dumbser, C.-D. Munz, R. Schneider, A high-order discontinuous galerkin method with time-accurate local time stepping for the maxwell equations, International Journal of Numerical Modelling: Electronic Networks, Devices and Fields 22 (1) (2009) 77–103.
- [20] T. Toulorge, W. Desmet, Cfl conditions for runge–kutta discontinuous galerkin methods on triangular grids, Journal of Computational Physics 230 (12) (2011) 4657–4678.
- [21] P. Gerhard, P. Helluy, V. Michel-Dansac, Unconditionally stable and parallel discontinuous galerkin solver, Computers & Mathematics with Applications 112 (2022) 116–137.
- [22] T. Weiland, A discretization model for the solution of maxwell’s equations for six-component fields, Archiv Elektronik und Uebertragungstechnik 31 (1977) 116–120.
- [23] T. Weiland, On the numerical solution of maxwell’s equations and applications in the field of accelerator physics, Part. Accel. 15 (DESY-84-006) (1984) 245–292.

- [24] T. Weiland, Time domain electromagnetic field computation with finite difference methods, *International Journal of Numerical Modelling: Electronic Networks, Devices and Fields* 9 (4) (1996) 295–319.
- [25] C. Carstensen, S. Funken, W. Hackbusch, R. W. Hoppe, P. Monk, *Computational Electromagnetics: Proceedings of the GAMM Workshop on Computational Electromagnetics*, Kiel, Germany, January 26–28, 2001, Vol. 28, Springer Science & Business Media, 2012.
- [26] D. Aregba-Driollet, R. Natalini, Discrete kinetic schemes for multidimensional systems of conservation laws, *SIAM Journal on Numerical Analysis* 37 (6) (2000) 1973–2004.
- [27] K. Xu, A gas-kinetic bgk scheme for the navier–stokes equations and its connection with artificial dissipation and godunov method, *Journal of Computational Physics* 171 (1) (2001) 289–335.
- [28] K. Xu, Gas-kinetic schemes for unsteady compressible flow simulations, *Computational Fluid Dynamics, Annual Lecture Series*, 29 th, Rhode-Saint-Genese, Belgium (1998).
- [29] S. Succi, *The Lattice Boltzmann Equation for Fluid Dynamics and Beyond*, Oxford University Press, 2001.
- [30] Z. Guo, C. Shu, *Lattice Boltzmann method and its application in engineering*, Vol. 3, World Scientific, 2013.
- [31] S. D. Pautz, An algorithm for parallel sn sweeps on unstructured meshes, *Nuclear Science and Engineering* 140 (2) (2002) 111–136.
- [32] P. J. Coelho, Advances in the discrete ordinates and finite volume methods for the solution of radiative heat transfer problems in participating media, *Journal of Quantitative spectroscopy and Radiative transfer* 145 (2014) 121–146.
- [33] C. Liu, K. Xu, A unified gas kinetic scheme for continuum and rarefied flows v: multi-scale and multi-component plasma transport, *Communications in Computational Physics* 22 (5) (2017) 1175–1223.
- [34] P. Gerhard, P. Helluy, V. Michel-Dansac, B. Weber, Parallel kinetic schemes for conservation laws, with large time steps, *Journal of Scientific Computing* 99 (1) (2024) 5.
- [35] S. Chapman, T. G. Cowling, *The mathematical theory of non-uniform gases: an account of the kinetic theory of viscosity, thermal conduction and diffusion in gases*, Cambridge university press, 1990.
- [36] R. Sanders, K. H. Prendergast, The possible relation of the 3-kiloparsec arm to explosions in the galactic nucleus, *Astrophysical Journal*, Vol. 188, pp. 489-500 (1974) 188 (1974) 489–500.
- [37] K. Xu, L.-S. Luo, Connection between lattice-boltzmann equation and beam scheme, *International Journal of Modern Physics C* 9 (08) (1998) 1177–1187.
- [38] P. J. Dellar, Lattice kinetic schemes for magnetohydrodynamics, *Journal of Computational Physics* 179 (1) (2002) 95–126.

- [39] F. Bouchut, Construction of bgk models with a family of kinetic entropies for a given system of conservation laws, *Journal of statistical physics* 95 (1999) 113–170.
- [40] T.-P. Liu, Hyperbolic conservation laws with relaxation, *Communications in Mathematical Physics* 108 (1987) 153–175.
- [41] P. Colella, Multidimensional upwind methods for hyperbolic conservation laws, *Journal of computational physics* 87 (1) (1990) 171–200.
- [42] B. Graille, Approximation of mono-dimensional hyperbolic systems: A lattice boltzmann scheme as a relaxation method, *Journal of Computational Physics* 266 (2014) 74–88.
- [43] Y. Zhu, C. Zhong, K. Xu, Numerical transport process of splitting kinetic schemes in the navier–stokes–fourier limit, *International Journal of Computational Fluid Dynamics* 35 (8) (2021) 653–665.
- [44] D. M. Sullivan, *Electromagnetic simulation using the FDTD method*, John Wiley & Sons, 2013.
- [45] J. S. Shang, D. In this case, the power is scattered much more in the forward direction. Gaitonde, Scattered electromagnetic field of a re-entry vehicle, *Journal of Spacecraft and Rockets* 32 (2) (1995) 294–301.